THE ASTROPHYSICAL JOURNAL, 465:127–144, 1996 July 1

MONTE CARLO SIMULATIONS OF DUSTY SPIRAL GALAXIES: EXTINCTION AND POLARIZATION PROPERTIES

SIMONE BIANCHI
Dipartimento di Astronomia e Scienza dello Spazio, Università di Firenze, Largo Enrico Fermi 5, I-50125 Firenze, Italy; sbianchi@arcetri.astro.it

AND

ANDREA FERRARA AND CARLO GIOVANARDI
Osservatorio Astrofisico di Arcetri, Largo Enrico Fermi 5, I-50125 Firenze, Italy
Received 1995 October 25; accepted 1996 January 11

ABSTRACT

We present Monte Carlo simulations of dusty spiral galaxies, modeled as bulge-plus-disk systems, aimed at studying their extinction and polarization properties. The extinction parameters (absorption and scattering) of dust grains are calculated from Mie's theory for a full distribution of sizes and materials; the radiative transfer is carried out for the four Stokes parameters. Photometric and polarimetric maps of galaxies of different optical depths, inclinations, and bulge-to-total luminosity ratios have been produced in the B and I bands. As expected, the effect of scattering is to reduce substantially the extinction for a given optical depth, in particular concerning the obscuration of bright bulge cores. For the same reason, scattering also reduces the reddening, as evaluated from $B-I$ maps. On the other hand, the blueing directly due to forward scattering is hardly appreciable. Radial color gradients are often found. A comparison with "sandwich" models shows that they dramatically fail to reproduce the extinction–optical depth relation. The degree of linear polarization produced by scattering is usually of the order of a few percent; it increases with optical depth and with inclination ($i \leq 80°$). The polarization pattern is always perpendicular to the major axis unless the dust distribution is drastically modified. There is little local correlation between extinction and polarization degree, and there is a trend of increasing polarization from the B to the I band. We discuss the implications and relevance of the results for studies of the structure and morphology of spiral galaxies and of their interstellar mediums.

Subject headings: dust, extinction — galaxies: ISM — galaxies: spiral — polarization — radiative transfer — scattering

1. INTRODUCTION

For a long time, since Holmberg's first analysis (Holmberg 1958), disk galaxies, including the gas-rich late morphological types, have been taken to be largely transparent systems. With various refinements, this point of view has been shared by the authors of catalogs of galaxies, such as the relatively recent Revised Shapley-Ames Catalog of Bright Galaxies (Sandage & Tammann 1981), and thereby adopted by the majority of the astronomical community. Holmberg inferred average values of the internal extinction on statistical grounds, that is, by interpreting the correlation between inclination and mean surface brightness in a rather limited sample of 119 spirals of various morphologies. On the other hand, refined studies of the dust content and distribution of individual, representative galaxies are scarce. In the edge-on Sc galaxy NGC 891, Kylafis & Bahcall (1987) were able to determine an overall transparency of the disk, when seen face-on, in a bandpass around 6000 Å.

Recently, however, some studies have shaken the widespread belief in transparent disks (Disney, Davies, & Phillipps 1989; Valentijn 1990), and the issue has rapidly become one of the most contended in the literature on normal galaxies, sometimes with opposite conclusions being drawn from analysis of the same or similar sets of data (Valentijn 1994). The idea of opaque galaxies has gained in the last years a certain acceptance and has been shared by the recent Third Reference Catalogue of Bright Galaxies (de Vaucouleurs et al. 1991).

This debate on the optical thickness of galactic disks is relevant to a number of issues important for extragalactic astronomy. We mention (1) the morphology and internal structure of galactic components, such as bulges, disks, lenses, and bars; (2) the dark matter content of galaxies and clusters; and (3) the luminosity corrections affecting redshift-independent measures of distance. This last point, in particular, touches on the field of the large-scale structure of the universe, and of the deviations from the Hubble flow.

For these reasons, observations and data analyses are becoming more refined, with particular reference to selection biases (Burstein, Haynes, & Faber 1991), redshift information (Chołoniewski 1991; Giovanelli et al. 1994), and multiwavelength imaging (Peletier et al. 1994; Evans 1994). At the same time, modeling has also become increasingly sophisticated. In fact, as has been argued by most of the authors cited above, a fundamental problem in statistical evaluations of the extinction lies in the absence of accurate and sensitive observable indicators. Surface brightnesses, diameters, and colors have often been interpreted in the framework of models so naive and unrealistic as to yield too-simplistic and sometimes wrong results.

A realistic modeling of dusty disks is thus strongly required. Besides, if we postulate the possibility of large optical thicknesses and sizable grain albedos, as is the case for wavelengths shorter than 3 μm, then the effects of multiple scattering in composite (bulge plus disk) systems, with dust interspersed with stars, must be included (see, e.g., Block et al. 1994). Remarkable progress along this track

was achieved in the recent paper by Byun, Freeman, & Kylafis (1994, hereafter BFK), who produced simulations of disk galaxies of various morphologies and optical thicknesses. Their treatment of radiative transfer includes the contribution of the first scattering exactly and the higher scattering orders approximately. They adopted a Henyey-Greenstein phase function and a single dust grain with average optical properties according to Draine & Lee (1984).

Scattering events are also expected to introduce polarization in the otherwise unpolarized emission from normal stars. Polarimetric studies of normal spirals, both observational and theoretical, are scarce. In view of the current interest in the properties of dusty disks, such scarcity is remarkable since most of the information about the physical properties of dust grains is locked into their polarization effects. Among the few observations of this kind, we mention the detailed studies of M31, M82, M104, and the Magellanic Clouds; they are summarized and referenced by Wielebinski & Krause (1993).

One of the fields in which the analysis and simulation of polarization maps has been most effective in recent years is star formation, in particular the study of protostellar envelopes (see Fischer, Henning, & Yorke 1994 and references therein). Here the more recent and detailed models are based on Monte Carlo simulations that allow for arbitrary distributions of polydispersive mixtures of spherical dust particles. In all these models, any observed polarization is imputed to transfer effects on light that is otherwise unpolarized when emitted by stars. In particular, since dust grains are usually assumed to be spherical, homogeneous, and optically isotropic, only the polarizing effect of scattering is taken into account. It is widely known, however, that in our Galaxy the linear polarization introduced by light's propagation through the interstellar medium is best described as the effect of dichroic absorption by aligned, elongated grains (Spitzer 1978; Gledhill & Scarrott 1989). Sometimes this polarization mechanism has been questioned, but, indeed, only for particular situations in which the presence of a suitable toroidal magnetic field, the main ingredient for the alignment, is dubious or improbable (Menard 1989).

We present here the results of Monte Carlo simulations of realistic model galaxies within the framework of Mie's scattering theory; that is, for spherical dust grains with homogeneous and isotropic optical properties. In our study, the dust grain is not a single, average one, but instead we allow for a mixture of different materials and a continuous distribution of size. The phase function is consistently computed from Mie's theory for each grain. The radiative transfer is exact to any scattering order and complete for the four Stokes parameters, so the output can be analyzed in the form of polarimetric, as well as photometric, maps. The three-dimensional distributions of stars and dust are the ones commonly accepted, and similar to those adopted by BFK. The present paper deals only with scattering events on spherical grains and does not include any dichroism in the absorption itself. The polarization properties may therefore be different from those that would be produced by needles rotating, as widely believed, in a galactic meridian plane.

Although we deal in this study with the simplest of the realistic cases, that is, smooth distributions and spherical grains, the Monte Carlo method is ideal for probing more hostile situations. The effects of clumping in the obscuring dust, of nonspherical dust grains, and of extinction by gas at short wavelengths are deferred to future papers.

2. DUSTY GALAXY MODEL

In the following, we describe the model distributions adopted here to simulate the spatial distribution of the photon emitters (stars) and the particles contributing to extinction (dust).

2.1. *Stellar Distributions*

We describe the stellar spatial distribution in a spiral galaxy by two components: a spheroidal bulge and a three-dimensional disk. We neglect dark, massive halos, since we are only interested in luminous components, and also possible small-scale inhomogeneities such as spiral arms and star-forming regions.

2.1.1. *Bulge*

The surface brightness profiles of spheroidal systems are usually well described by the $R^{1/4}$ law (de Vaucouleurs 1959):

$$I(R) = I_e 10^{-3.33[(R/R_e)^{1/4}-1]}, \quad (1)$$

where R_e is the equivalent radius and I_e is the surface brightness of the corresponding isophote; both R and R_e are measured on the sky plane. For numerical purposes, it is convenient to have an analytical expression for the bulge luminosity density $\rho^{(b)}$, which can be obtained by deprojecting the profiles. Since there is no simple analytical expression for $\rho^{(b)}$ corresponding to equation (1) (see Young 1976), we chose to adopt the Jaffe distribution, which corresponds to the luminosity density (Jaffe 1983):

$$\rho^{(b)}(\tilde{r}) = \frac{\rho_0^{(b)}}{(\tilde{r}/r_b)^2[1 + (\tilde{r}/r_b)]^2}, \quad (2)$$

where $\tilde{r}$ is the physical distance from the galactic center and r_b is the scale radius, for which we adopt $r_b = 1.16R_e$ (see Appendix, § A1.1).

In principle, there is no need for an external truncation radius for the Jaffe distribution since the volume integral converges for $\tilde{r} \to \infty$; for numerical purposes, though, we have introduced a truncation radius $r_{\max}^{(b)} = nr_b$. In fact, in the absence of an external truncation, at large radii the bulge's light will dominate once again that of the (exponential) disk. In the simulations presented here, we have adopted the values $R_e = 1.60$ kpc, $n = 8$. This value for R_e is close to that inferred for our Galaxy; the value for n is such that $r_{\max}^{(b)}$ corresponds to the point where the ratio between the bulge luminosity density and the density of the adopted disk is maximum (§ 2.1.2).

2.1.2. *Disk*

The assumed luminosity density distribution for the disk is

$$\rho^{(d)}(r, z) = \rho_0^{(d)} \exp(-r/r_d) Z(z/z_d) \quad (3)$$

(Freeman 1970), where r and z are the cylindrical radius and the height above the equatorial plane of the galaxy, respectively, and the constants r_d and z_d are the relative scale lengths. The function $Z(z/z_d)$ describes the vertical behavior of the distribution, which is assumed to be either exponential or of the "sech^2" type (see van der Kruit & Searle 1981; Wainscoat, Freeman, & Hyland 1989); the results presented

in this paper are for the exponential vertical distribution,

$$Z(z/z_d) = \exp(-|z|/z_d) . \quad (4)$$

In analogy with the bulge case, we have introduced a horizontal, $r_{\max}^{(d)} = mr_d$, and a vertical, $z_{\max}^{(d)} = kz_d$, external truncation. Our models are for $r_d = 4.0$ kpc, $z_d = 0.35$ kpc, which are similar to the values observed for the old disk population of the Galaxy; for the external truncations we adopt $m = k = 6$.

2.1.3. *Bulge-to-Total Luminosity Ratios*

To simulate different Hubble types, we have run models with different bulge-to-total luminosity ratios (B/T), ranging from 0 (resembling an Sd galaxy, model BT00) to 0.5 (Sa, model BT05). All our simulations are monochromatic, and we have run models at the effective wavelengths of the B and I bandpasses, 4400 and 9000 Å, respectively. Possible differences in the stellar populations of the two components are taken into account by adopting for the bulge a $B-I$ color larger than that of the disk. More precisely, the luminosity of the bulge has been increased by 1 mag in the I band while the luminosity of the disk has been kept constant in both bands, i.e., we suppose an intrinsic $B-I = 0$ for the disk and $B-I = 1$ for the bulge.

All of these prescriptions conform to those adopted by BFK.

2.2. *Dust Properties*

The only absorbing particles included in our code are dust grains; we neglect the absorption above the Lyman limit due to diffuse hydrogen gas and the possible presence of molecules.

2.2.1. *Dust Disk*

The dust is assumed to be smoothly[1] distributed in a disk according to the same law (eq. [3]) as for the stellar disk,

$$\rho^{(g)}(r, z) = \rho_0^{(g)} \exp(-r/r_g) Z(z/z_g) , \quad (5)$$

where r_g and z_g are the horizontal and vertical dust scale lengths. In this paper we are mainly interested in determining the effects of a *standard* dust layer on the structural parameters and appearance of a galaxy; we will devote a following paper to study of the detailed structure and distribution of dust as inferred from the observed light distributions in spiral galaxies. The Galactic parameters are by far more uncertain for the dust distribution than for the stars. For the computations presented here, we have assumed $r_g = 4.0$ kpc, $z_g = 0.14$ kpc, and the same truncation factor as for the stellar disk. That is, while the radial extents of the stellar and dust disks are identical, we will always deal with dust disks that are vertically embedded in the stellar distribution. This is an important point, since several of the results that follow will be determined by the presence of sizable stellar emission outside the obscuring layer.

We assume that the dust's physical properties (the distribution of grain size and materials; see below) are independent of position in the galaxy and therefore that the absorption coefficient at wavelength λ can be written as $k_\lambda = \langle C^{\rm ext}(\lambda)\rangle \rho^{(g)}(r, z)$, where $\langle C^{\rm ext}(\lambda)\rangle$ is the extinction cross section per unit mass, averaged over the grain distribution and materials (see eq. [7]).

[1] A study of the effects introduced by dust clumping is in progress.

It is common to normalize the total content of dust in a galaxy in terms of the optical depth along the symmetry axis of the galaxy,

$$\tau_\lambda(0) = \int_{-\infty}^{\infty} C^{\rm ext}(\lambda)\rho^{(g)}(r = 0, z)\, dz = 2\langle C^{\rm ext}(\lambda)\rangle \rho_0^{(g)} z_g , \quad (6)$$

for both the exponential and sech^2 distributions. As in the case of the stellar disk, the results presented here refer to vertically exponential dust disks.

2.2.2. *Dust Components and Size Distribution*

In our models, the grains are assumed to be spherical and to have a size distribution as given by the MRN model (Mathis, Rumpl, & Nordsiek 1977), $n(a) \propto a^{-3.5}$, where a is the grain radius. We consider three materials: astronomical silicates, $\|$-graphite, and $\perp$-graphite. The numerical silicates-to-graphite ratio is 1:1.12, with one-third of the graphite having optical properties measured parallel ($\|$), and two-thirds perpendicular ($\perp$), to the c-axis. The lower and upper limits of the distribution are $a_- = 0.005$ μm and $a_+ = 0.25$ μm, irrespective of the material. Very small grains and polycyclic aromatic hydrocarbons have not been included, because of the large uncertainties in both their size distribution and optical constants.

The dielectric constants adopted are the ones given by Draine & Lee (1984), recently extended into the far-UV and X-ray by Martin & Rouleau (1991). All the relevant optical properties (absorption and scattering cross sections, albedo, phase function, and Mueller matrix) have been calculated using Mie formulae. The resulting extinction curve is illustrated in Figure 1.

The central optical depth of the disk in our models is defined by $\tau_V(0)$, the value at 5500 Å; models at different wavelengths are still defined by $\tau_V(0)$, but all computations of optical thickness were scaled according to our extinction curve.

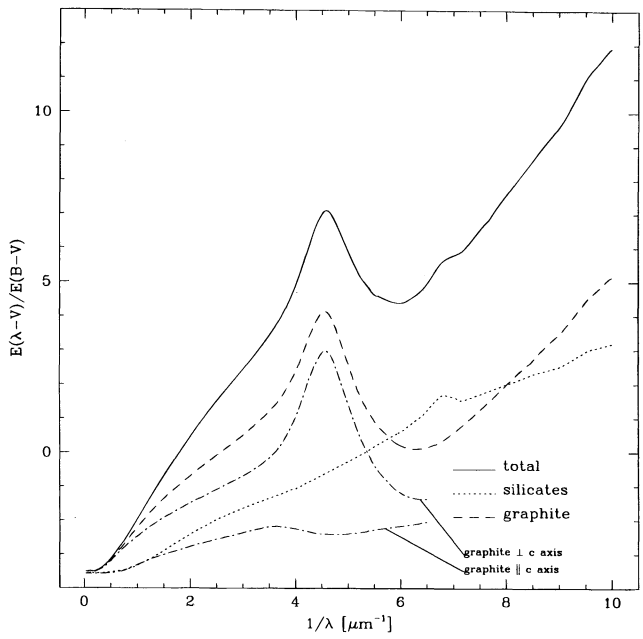

FIG. 1.—Extinction curve resulting from the adopted dust model. Also shown are the contributions of the single components. The color excesses for the single materials are divided by the value of $E(B-V)$ for the total mixture.

2.2.3. *Comparison with the Henyey-Greenstein Approximation*

The average value of a quantity q over the dust distribution is defined here as

$$\langle q \rangle = \frac{\sum_i w_i \int_{a-}^{a+} q C_i^{\rm ext} n_i(a)\, da}{\sum_i w_i \int_{a-}^{a+} C_i^{\rm ext} n_i(a)\, da}, \quad (7)$$

where $C_i^{\rm ext}$ is the extinction cross section, the index i refers to the material, and w_i is its weight in the distribution; both q and $C_i^{\rm ext}$ depend on λ.

Previous works dealing with scattering problems have often approximated the phase function Φ with the Henyey-Greenstein (H-G) formula,

$$\Phi(\theta, \phi) = \frac{1}{4\pi} \frac{1 - g^2}{(1 + g^2 - 2g \cos \theta)^{3/2}} \quad (8)$$

(Henyey & Greenstein 1941), where g is the asymmetry parameter (i.e., the average value of cos θ weighted by the phase function) and θ and ϕ are the polar and azimuthal scattering angles, respectively. In Figure 2, we show a comparison between the average phase function for the distribution calculated with the Monte Carlo procedure implemented in our radiative transfer code and the H-G phase function, for which a value of g averaged over the distribution according to equation (7) has been used upon substitution of $C_i^{\rm ext}$ with $C_i^{\rm sca}$, the scattering cross section. The differences between the two phase functions are not striking (the B and I bands are shown as an example)—the H-G approximation always underestimates the forward scattering, by about 5%, the difference being larger in the B band.

For the albedo and asymmetry parameters, we obtain $\langle \tilde{\omega} \rangle = 0.53$ and $\langle g \rangle = 0.48$ in the B band and $\langle \tilde{\omega} \rangle = 0.50$ and $\langle g \rangle = 0.30$ in the I band.

3. MONTE CARLO SIMULATION

Monte Carlo methods allow the life of each photon to be followed through scattering and absorption processes. Here we provide a brief description of our computational scheme, referring the interested reader to the Appendix for a more detailed presentation.

3.1. *Emission Cycle*

We first determine the position of the photon emission point according to the bulge and disk luminosities described in § 2.1. Photons are emitted isotropically and without polarization. The Stokes parameters are defined for each photon on the plane perpendicular to its propagation vector, following the conventions in Shurcliff (1962); the reference direction on such plane is the projection of the galactic z-axis (i.e., the symmetry axis). All photons are emitted with the same intensity, or strength, i.e., with the first Stokes parameter $I = 1$. The emission cycle requires five random numbers: three for the position and two for the direction (see Appendix, § A1).

3.2. *Scattering Cycle*

Next, we determine the position of the scattering point, i.e., the position at which the photon collides with a dust grain; grains are assumed to be distributed as described in § 2.2. This implies the determination first of an optical depth τ for the scattering point and then of the geometrical position along the line of propagation at which this τ is actually reached. It turns out that this second step is computationally the most time-consuming of the whole process (Appendix, § A2). Once the position of the scattering event is known, we pass on to determining the characteristics of the dust grain, according to the size and composition distributions (Appendix, § A3). Note that, in principle, such a sequence renders rather straightforward the consideration of situations in which the physical properties of dust vary within the galaxy, e.g., with galactocentric distance. These steps require two more random numbers, one to locate the diffusion point and the other to fix the size and composition

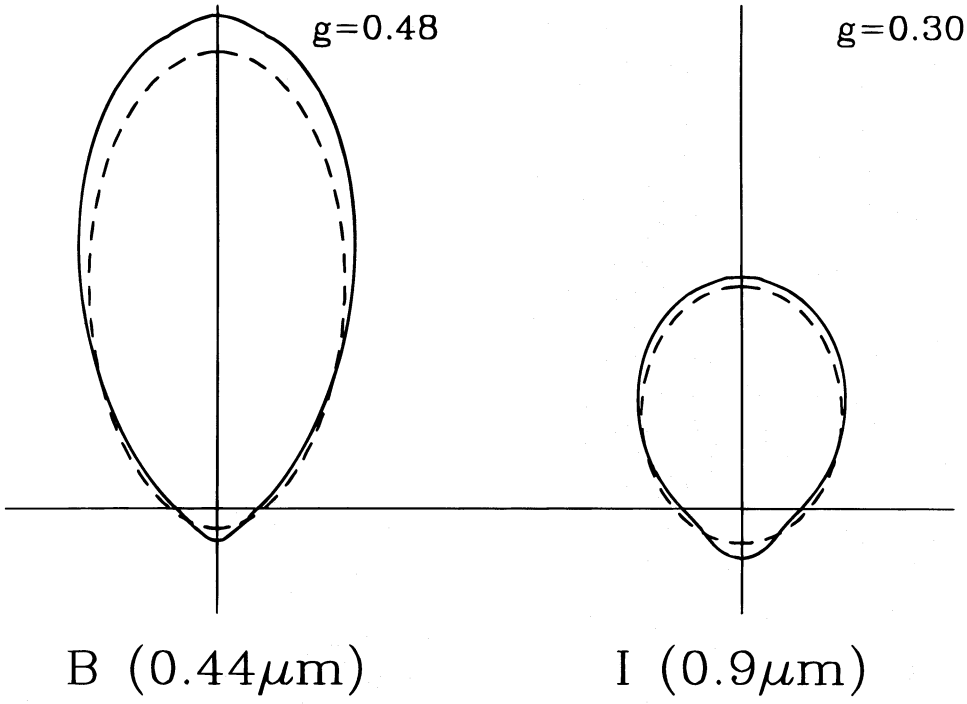

FIG. 2.—Average phase functions as computed by the Monte Carlo code (*solid lines*) and H-G phase functions with g corresponding to the mean value for the same dust distribution (*dashed lines*); the phase functions are shown at the central wavelengths of the B and I bandpasses.

of the scatterer. Knowing the radius and refractive index of the grain (together with λ), it is now possible to compute the (polar) phase function and the albedo and, by extracting a new random number, to choose the (polar) angle of scattering, θ. Together with the geometrical and optical properties of the dust grain, within the framework of Mie's theory, θ completely determines the elements of the scattering (Mueller) matrix. The matrix elements also enter into the expression for the azimuthal phase function, so by extracting a new, final, random number, we define completely the direction and Stokes vector of the scattered photon (see Appendix, § A4).

The updated Stokes parameters are calculated via the transformation

$$\begin{pmatrix} I' \\ Q' \\ U' \\ V' \end{pmatrix} \propto \mathbf{R}'\mathbf{M}\mathbf{R} \begin{pmatrix} I \\ Q \\ U \\ V \end{pmatrix}. \quad (9)$$

The rotation matrix **R** transforms the initial Stokes parameters into a new set whose reference direction for linear polarization lies in the scattering plane. **M** is the relevant Mueller matrix with respect to the scattering plane, which depends only on θ and the dust properties; the matrix $\mathbf{R}'$ provides the final transformation of the Stokes parameters to the final reference direction, that is, the projection of the z-axis onto the plane normal to the new direction of propagation. In our formulation we make use of normalized Mueller matrices; the absolute values of the Stokes parameters are adjusted according to the incoming intensity I and to the albedo of the scatterer. In summary, a single scattering cycle requires the extraction of four random numbers: one to locate the diffusion point, one to choose the size and type of grain, and two for the direction of the scattered photon. The scattering cycle is iterated until the photon escapes the dust layer or dies because its strength, I, falls below a threshold value ($I_{\rm lim} = 10^{-4}$).

3.3. *Output and Performance*

The output of the code consists of N_B maps for each Stokes parameter, where N_B is the number of bands of different galactic inclination to the line of sight (Appendix, § A5). The models presented here were obtained with $N_B = 15$, and each map has an extent of 201 × 201 pixels with a spatial resolution of 0.2 kpc; the resolution is therefore moderate in both space and inclination.

A full model (bulge plus disk) with enough signal-to-noise ratio (S/N) to distinguish a clear polarization pattern in the outer parts of the galaxy (with linear polarization degree of $\sim 1\%$) requires a number of photon launches of the order of 10^8. In any case, photometric accuracies comparable to those of astronomical images are usually attainable with less than 10^7 launches. The code has been tested on a variety of more simple and predictable situations: point sources within spherical scattering envelopes, Rayleigh scattering, optically thin regimes, and absorption only.

4. RESULTS

In summary, the models presented here were all obtained for bulge effective radius $R_e = 1.6$ kpc, truncated at 15 kpc; disk radial scale length $r_d = 4.0$ kpc, truncated at 24 kpc; disk exponential vertical scale length $z_d = 0.35$ kpc, truncated at 2.1 kpc; dust radial scale length $r_g = 4.0$ kpc, truncated at 24 kpc; and dust exponential vertical scale length $z_g = 0.14$ kpc, truncated at 0.84 kpc. None of the results obtained depend on the adopted truncation factor as far as they exceed 5 scale lengths.

We ran simulations for six different values of $\tau_V(0)$: 0.0, 0.5, 1.0, 2.0, 5.0, 10.0; and for four different B/Ts: 0.0, 0.1, 0.3, 0.5. The average angles[2] to the line of sight of the eight independent inclination bands were $\langle\theta\rangle = 20°$, 37°, 48°, 58°, 66°, 75°, 82°, and 90°.

All of these models were produced both at 4400 Å, for the B band, and at 9000 Å, for the I band. We also ran some simulations, although not a complete set, at 3500 Å (U band).

4.1. *Extinction Properties*

Since the adopted range of parameters conforms to those used by BFK, we can directly compare our results with theirs. All the results about minor- and major-axis profiles,[3] total extinction, face-on corrections, and isophote shapes and diameters agree remarkably well, and therefore we refer the reader to their work (for a more thorough discussion, see also Bianchi 1995). Most of differences between our results and those of BFK are ascribable to the choice of extinction law. While BFK used the empirical data of Rieke & Lebofsky (1985), which yield $A_B = 1.32A_V$, we conform to the MRN and Draine & Lee (1984) model (§ 2.2.2, Fig. 1) and obtain $A_B = 1.28A_V$. Additional differences arise from the finite spatial resolution of our images and the finite resolution in inclination to the line of sight, as explained in the Appendix (§ A5). However, these differences are relevant only when intensity varies greatly with position and inclination (the edge-on case).

We point out that the central surface brightness of disks with large optical depth still varies with inclination because of stars not immersed in dust if the dust's scale height is indeed smaller than for stars. In addition, in the B band, the difference between edge-on and face-on central surface brightness is the same for all models with $\tau_V(0) \geq 2$, which corresponds to 0.3 mag. This common behavior makes the study of central surface brightness unsuitable for determination of the optical depth of the dust disk in spiral galaxies. As for the influence of scattering, the main (and obvious) result is a substantial reduction of the actual extinction for a given $\tau_V(0)$. As illustrated in Figure 3, such reduction is higher for greater $\tau_V(0)$ and lower inclination, with a maximum of ~ 0.3 mag for B-band models. For edge-on models, the difference is less than 0.1 mag, so neglecting the effects of scattering when fitting the brightness profiles of highly inclined objects can be rather justified (see Ohta & Kodaira 1995).

4.1.1. *Local Extinction*

The differences between models that include scattering and models with absorption only can also be appreciated by analyzing the local extinction. In Figure 4, we plot the central ($r = 0$) extinction for models in the B band (A_B) with

[2] As defined by $\langle\theta\rangle_i = \int_{\theta_i^-}^{\theta_i^+} \theta \sin\theta\, d\theta$, where θ_i^- and θ_i^+ are the limiting values for the ith inclination band.

[3] The shape of the major-axis profiles of systems with conspicuous bulges, inclinations less than 80°, and $\tau_V(0) > 2$ closely resembles the type II profiles defined by Freeman (1970). In any event, as noted by the same author, they also often show up in galaxies with low dust content, such as S0's, and therefore their explanation seems to require peculiar stellar distributions in addition to extinction effects.

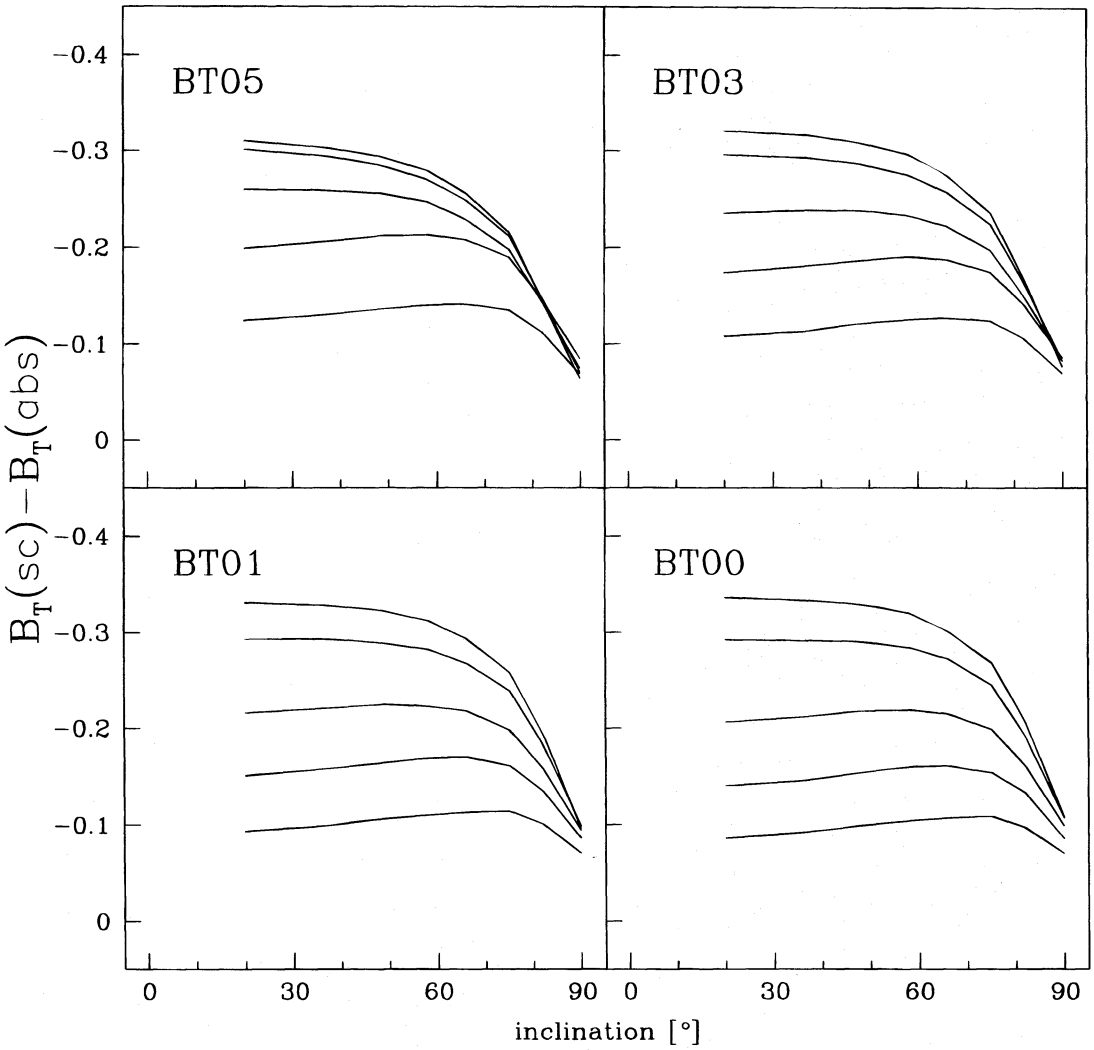

FIG. 3.—Difference in total B magnitude between models including scattering, B_T(sc), and with absorption only, B_T(abs), as a function of inclination for different B/Ts. In each panel, the five lines refer to different total opacities: $\tau_V(0) = 10,\ 5,\ 2,\ 1,\ 0.5$, from top to bottom.

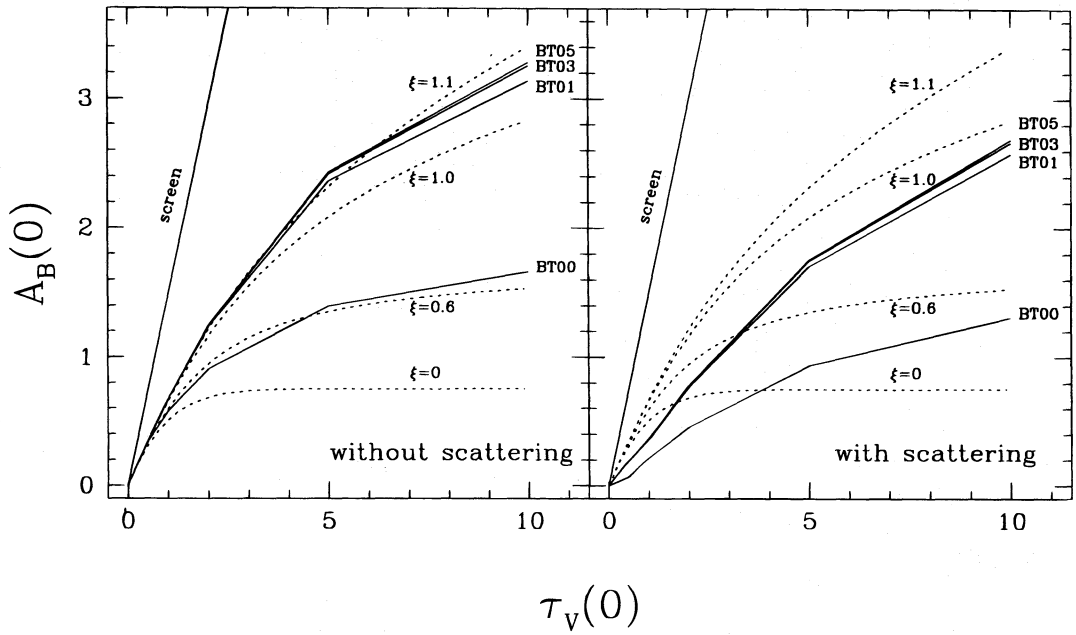

FIG. 4.—Central ($r = 0$) extinction vs. optical depth $\tau_V(0)$ for B models with $i = 20°$ (*solid lines*); the left panel is for models with absorption only, the right panel for absorption-plus-scattering models. Dotted lines refer to sandwich models with different dust-to-star thickness ratios (ξ). The straight solid line is for the screen model.

$i = 20°$ (our inclination nearest to face-on) as a function of the central optical depth, $\tau_V(0)$. The straight lines correspond to the Holmberg screen model, dotted ones to sandwich models (Disney et al. 1989) with different dust-to-stellar thickness ratios ξ. The left panel is for models with absorption only, while the right panel includes scattering; screen and sandwiches are the same in both panels and only include absorption.

Absorption-only models show that the behavior of the central extinction in the pure disk models (BT00) can be described locally by a sandwich with $\xi = 0.6$, while models that include a bulge require inverse sandwiches, that is, with dust extending higher than stars from the equatorial plane ($\xi = 1.1$). This is because the bulk of the emission at the center, i.e., the bulge core, is located inside the dust layer.

In models with scattering (*right panel*), we note that the central extinction is reduced by several tenths of a magnitude since the radiation has a good probability of being diffused by the dust rather than absorbed. This is because, with our assumptions about the dust's composition and size distribution, the average albedo amounts to ~ 0.5, both in the B and the I band. Moreover, the behavior of scattering models is very different from that of sandwiches.

In Figure 5, we show the extinction at $r = r_d$ on the major axis as a function of the local vertical optical depth, for the same models as in Figure 4. Since the bulge contribution is small at this distance, all the models present nearly the same behavior, principally regulated by the disk. Models with scattering show again that sandwiches are a poor approximation. It is interesting to note that for $\tau_V(0) < 0.5$, scattering plays such a role that extinction is basically absent.

4.1.2. *Images and Color Maps*

Intensity images and $B-I$ color maps yield additional information. In Figure 6, we show images in the B band and color maps for a bulge, a disk, and a BT05 model, with inclination 82° and $\tau_V(0) = 10$. Since the extinction for bulge and disk is due to the same dust disk, the BT05 model is simply a superposition of the first two images. We have used the same gray scale for the intensity images, while the color maps have different scales to evidence the details.

Extinction is more pronounced in the bulge because stars and dust are not homogeneously mixed and the dust acts almost like a screen. However, extinction also modifies the shape of the disk, which becomes asymmetric with respect to the major axis. Color maps are positive everywhere, in pure disks also (intrinsic $B-I = 0$), indicating a general reddening. The red color of the outer "halo" in the BT05 maps is due to the intrinsic ($B-I = 1$) color of the bulge (the different appearance is due to different gray scales).

The expected effect of scattering on colors is to render bluer the zones of an image where a substantial fraction of emerging radiation is contributed by forward scattering. This is due to the more asymmetric phase function at shorter λ (§ 2.2.2). This effect should be more evident in highly inclined objects and in the regions of the (dust) disk situated between the observer and the bright bulge core (Elvius 1956).

Analyzing the pure bulge color maps, we do note a less red lane near the center, coincident with the dust disk's plane, but still with $B-I \geq 1$. This "blue" lane cannot be accounted for by scattering effects since it is also present in models with absorption only. It is due, instead, to the heavy extinction of the central parts. Where this happens, the observed emission is mostly due to stars located out of the dust layer, and therefore the reddening is small. The reddest parts are in fact those where the local opacity (along the line of sight) is high but less than ~ 15. We note that when scattering is included, because of the lower effective opacity for a given $\tau_V(0)$, this effect is reduced and the central equatorial lane actually becomes redder. The disk presents this lane as well, but the contrast is not as strong; as an example, we show in Figure 7 the results along the major axis of a pure disk with $\tau_V(0) = 5$ at several inclinations; the right panel is for a model with scattering while the left is for pure absorption. The study of the color profile has been sug-

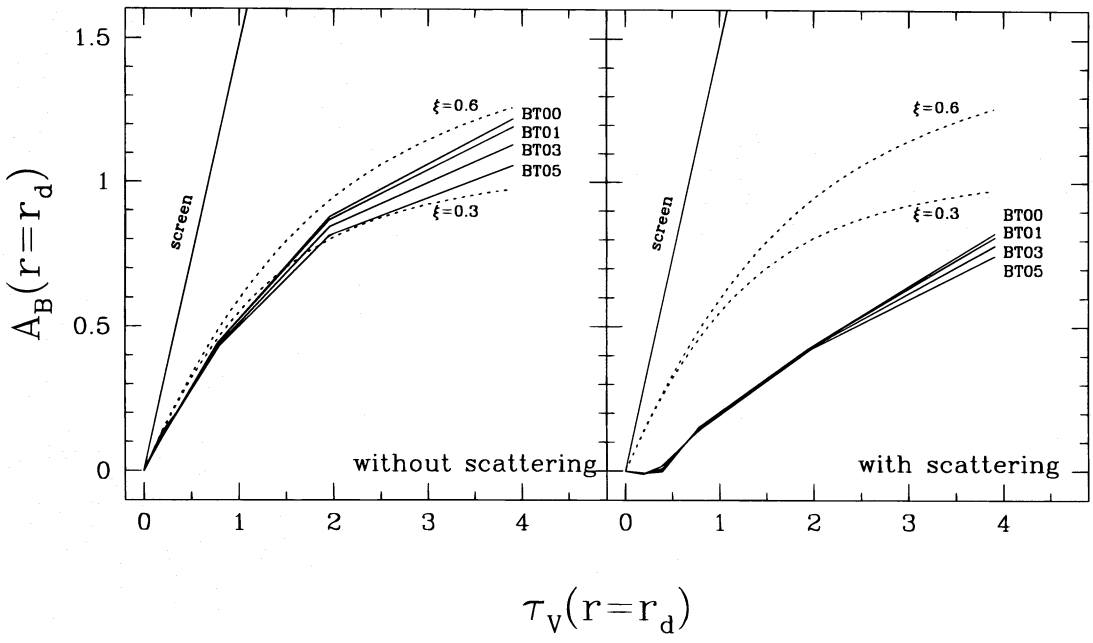

FIG. 5.—Same as Fig. 4, but for $r = r_d$

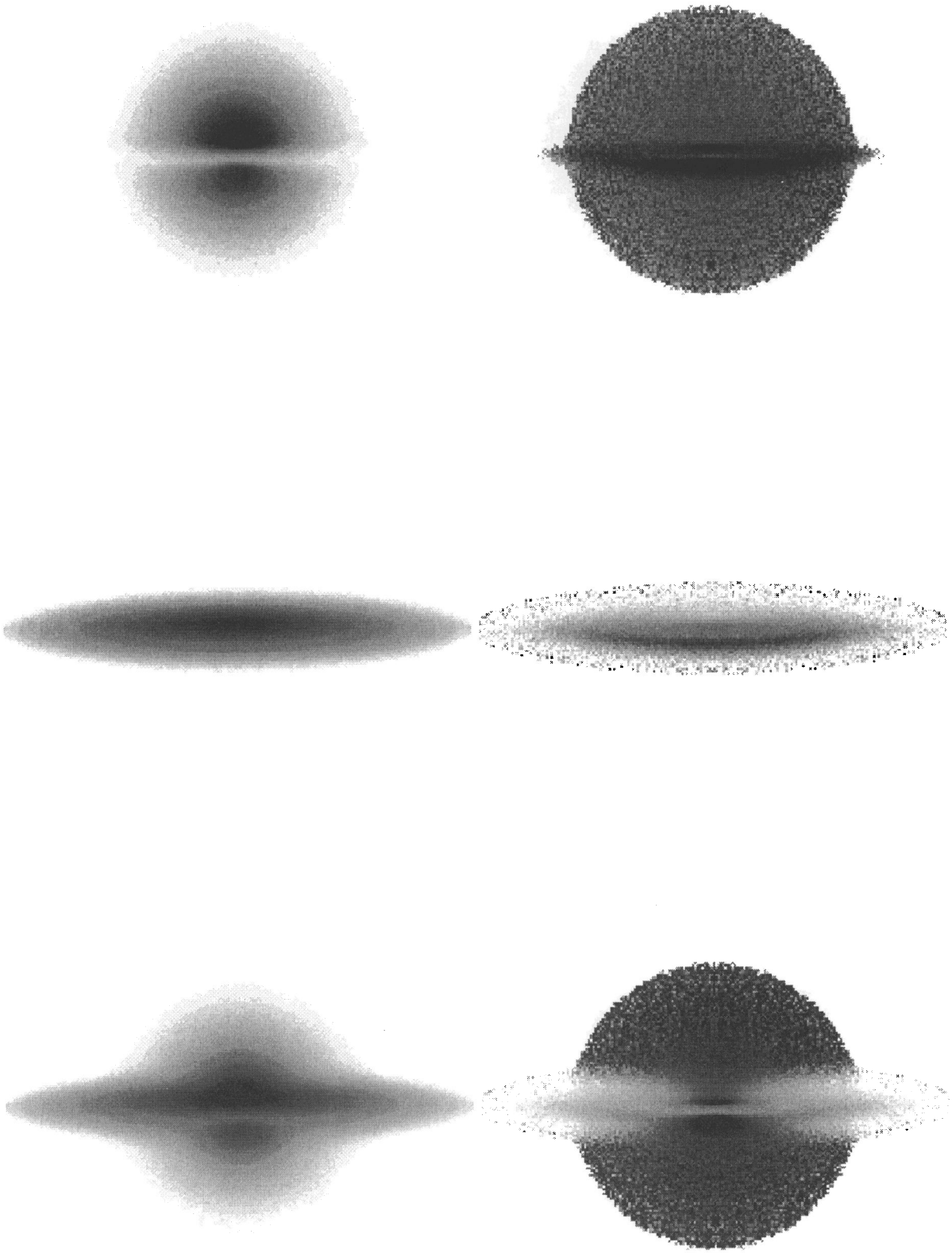

FIG. 6.—*B*-band images (*left*) and $B-I$ color maps (*right*) for a bulge (*top*), a disk (*center*), and a BT05 model (*bottom*) as seen from an inclination of 82°. The dust disk is the same in the three cases, with $\tau_V(0) = 10$.

gested by BFK as a possible tool to infer the (local) optical depth: color gradients are located in regions where the optical depth along the line of sight is ~ 1. Our models agree with this result. Besides, the shape of the color profiles, and the position of the gradients, is about the same with or without scattering; this means that pure absorption models can provide a sufficiently good τ-diagnostic.

We have also performed simulations in the U band. Scattering effects in this wavelength are similar to those in the B band, and therefore $U-B$ color maps are not appreciably

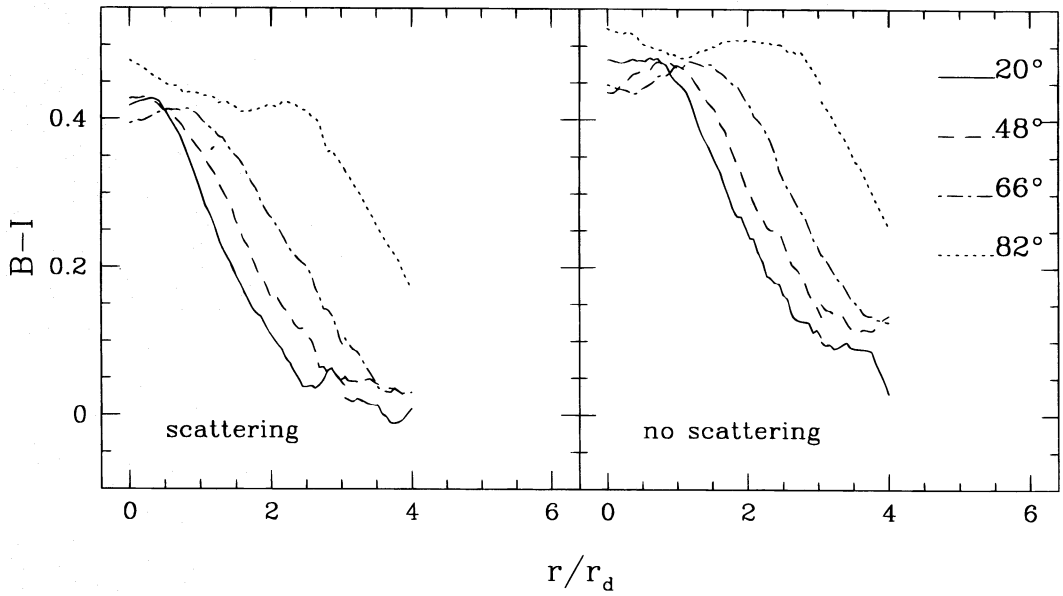

FIG. 7.—Color profiles along the major axis for a BT00 model (pure disk) with $\tau_V(0) = 5$ at several inclinations. *Left*, for models with only absorption; *right*, for absorption-plus-scattering models. Lines are truncated at $r = 4r_d$ because of the poor S/N at larger radii.

different from those obtained with simpler absorption models.

4.2. *Polarization Analysis*

We now examine the polarization properties of our models. The range of parameters explored is the same as for the surface brightness maps.

While the polarization introduced by a single scattering is usually conspicuous, it will be seen that the predicted degree of linear polarization is low (a few percent). This is due to three different causes:

1. Photons emerging from the same position in a map can be either *primitive*, unpolarized photons (emitted by stars and having escaped without being intercepted by dust) or scattered, polarized photons. The first cause of low polarization is, therefore, the dilution by primitive radiation, which is higher in the regions of higher surface brightness, such as the central parts of both bulges and disks.

2. If we restrict ourselves to the contribution to a certain pixel of scattered photons only, the resultant polarization will be maximum if the scattered photons have similar histories. So, the requirement for a high degree of polarization is threefold: first, the main contribution must come from single-scattering events; second, photons must be scattered within a thin region along the line of sight; third, the scattering region must be illuminated from a narrow solid angle. The first and second requirements are usually met in the parameter range of our models. The third requires a compact stellar distribution with respect to the dust disk and is only met by the bulge component.

3. The polarization will obviously be highest if the scattering grains are identical. As mentioned previously, our models make use of a distribution in size and composition of grains, and to each size and composition, our code assigns, for a given scattering angle, a different Mueller matrix. As a result, photons emitted by the same star and scattered at the same point in the same direction may have quite different polarization properties, depending on the characteristics of the scattering grain.

The maps that we will examine are obtained by averaging the images for the several Stokes parameters within 10×10 pixel squares. This lower resolution has been necessary to compensate for the lower S/N figures of the polarization maps. In Figure 8 are collected the linear polarization maps in the *B* band at different inclinations for the emission from the bulge only, from the disk only, and from a composite BT05 model. The disk of dust is the same in all cases, namely, the one with highest optical depth, $\tau_V(0) = 10$.

The degree of polarization turns out to be higher for larger optical depths. For the BT05 model of Figure 8 at 75° inclination, the largest polarization degree is $\sim 1.5\%$; in the same conditions but with $\tau_V(0) = 0.5$, the maximum is 0.8%. The zones of highest polarization are always located on or near the major axis. Another notable feature of our models is that, while increasing $\tau_V(0)$, the location of the maximum polarization moves outward; this is illustrated by the sequences in Figure 9, which show the behavior of the polarization degree along the major axis with galactocentric distance for some of our models.

Clearly, for the reasons discussed above, the main contribution comes from scattering of the radiation from the bulge. This component has a more compact distribution, with an emissivity highly peaked at the center, which is seen by the scatterers in the disk almost as a point source. The case of a pure bulge best illustrates the dilution of polarization by direct radiation; the maximum degree of polarization does not vary appreciably with inclination.

Pure disks show very little polarization when seen face-on; this fact is mainly due to the rather flat distribution of disk stars. The polarization degree increases with inclination, with a maximum around 50°–80°, and then decreases again slightly as a result of the long line of sight through the disk when approaching 90°. As a rule, in composite models, the scattering of disk radiation will provide the polarization of the inner regions while the bulge will mainly polarize the

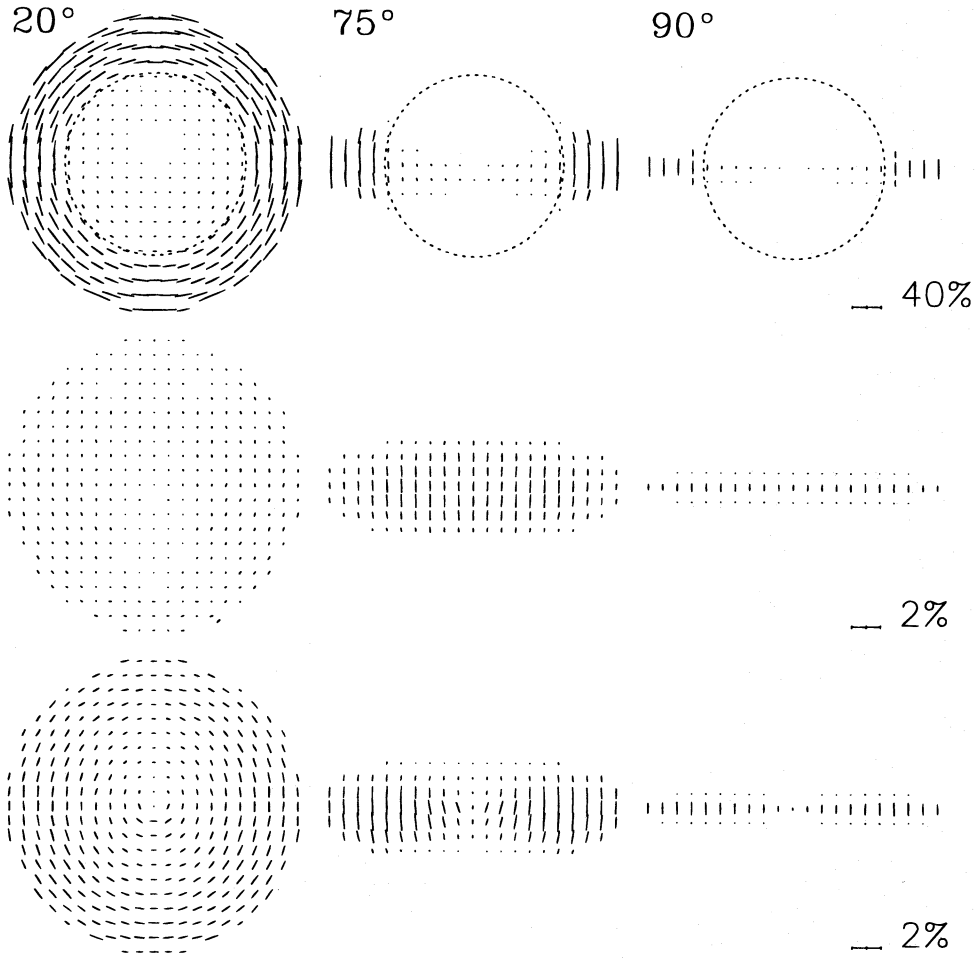

FIG. 8.—*B*-band polarization maps for a bulge (*top*), a disk (*middle*), and a BT05 model (*bottom*). The optical depth is $\tau_V(0) = 10$, and the inclinations are 20°, 75°, 90°, from left to right. The dust disk is the same in the three cases. For each model, the linear polarization scale is given on the right. The dashed circle in the upper maps corresponds to the extent of the bulge.

external disk. Note how the strong polarization of the outer disk in the case of a pure bulge ($\sim$30%) is diluted by direct disk light and reduced to 1.0%–1.5%. As a consequence, the morphology of the polarization pattern, when seen at favorable inclinations (50°–80°), is different in systems with different bulge luminosities: late spirals will have a more uniform elliptical pattern, and early ones a two-lobed structure aligned along the major axis.

As for the direction of the linear polarization vector, it is invariably aligned perpendicularly to the major axis. This means that, for the scattered field, the ***E*** component perpendicular to the plane of scattering, $E_\perp$, is higher than the parallel one, $E_\parallel$, for most of the directions with a sizable phase function. This is the situation commonly observed in scattering by small particles, where $x = 2\pi a/\lambda \ll 1$, as is the case, for example, in electron scattering. When dealing with dust grains with refractive indexes around 1, this is not the only possible situation. The pattern can be inverted, in principle, at larger values of x (see, e.g., Fig. 25 of van de Hulst 1957). We have performed a few simulations to check if, with larger grains or at smaller λ, the pattern would appreciably change, in the sense of a polarization pattern with a definite alignment along the equator, when seen edge-on. Our results indicate that for any reasonable dust composition and size distribution, this situation is difficult to achieve for $\lambda \geq 2000$ Å. The reason is that, at such wavelengths, the scattered field is mainly contributed by graphite ($\perp$) grains, which have a (real) refractive index $m \geq 2$. This requires, for a radical change in the pattern direction, values of $x \geq 1.5$, which means, in the visual ($\lambda = 5500$ Å), a lower cutoff $a_- \geq 0.13$ μm instead of the canonical $a_- = 0.005$ μm. The resulting polarization map for such a model is illustrated in Figure 10 (note the low polarization degree).

Another point to mention is the comparison between the polarization maps and the isophotal ones: two aspects are noticeable. First, although the brightest, inner parts show very little polarization, measurable values (>1%) are diffused over most of the galaxy's image, well inside 25 *B*-mag arcsec^{-2}, and, therefore, accessible to observations (Fig. 11). Second, for a given model and inclination, we find little spatial correlation between extinction and polarization, even in highly inclined models with large $\tau_V(0)$; for example, the equatorial dust lanes of highly inclined disks are not strongly polarized. This is another sign that polarization is mainly contributed by single-scattering events in the outer layers of the disk.

A clear prediction of our models concerns the wavelength dependence of the degree of linear polarization, which we find to increase from the *B* to the *I* band. This appears to be a general rule, independent of B/T, $\tau_V(0)$, and inclination.

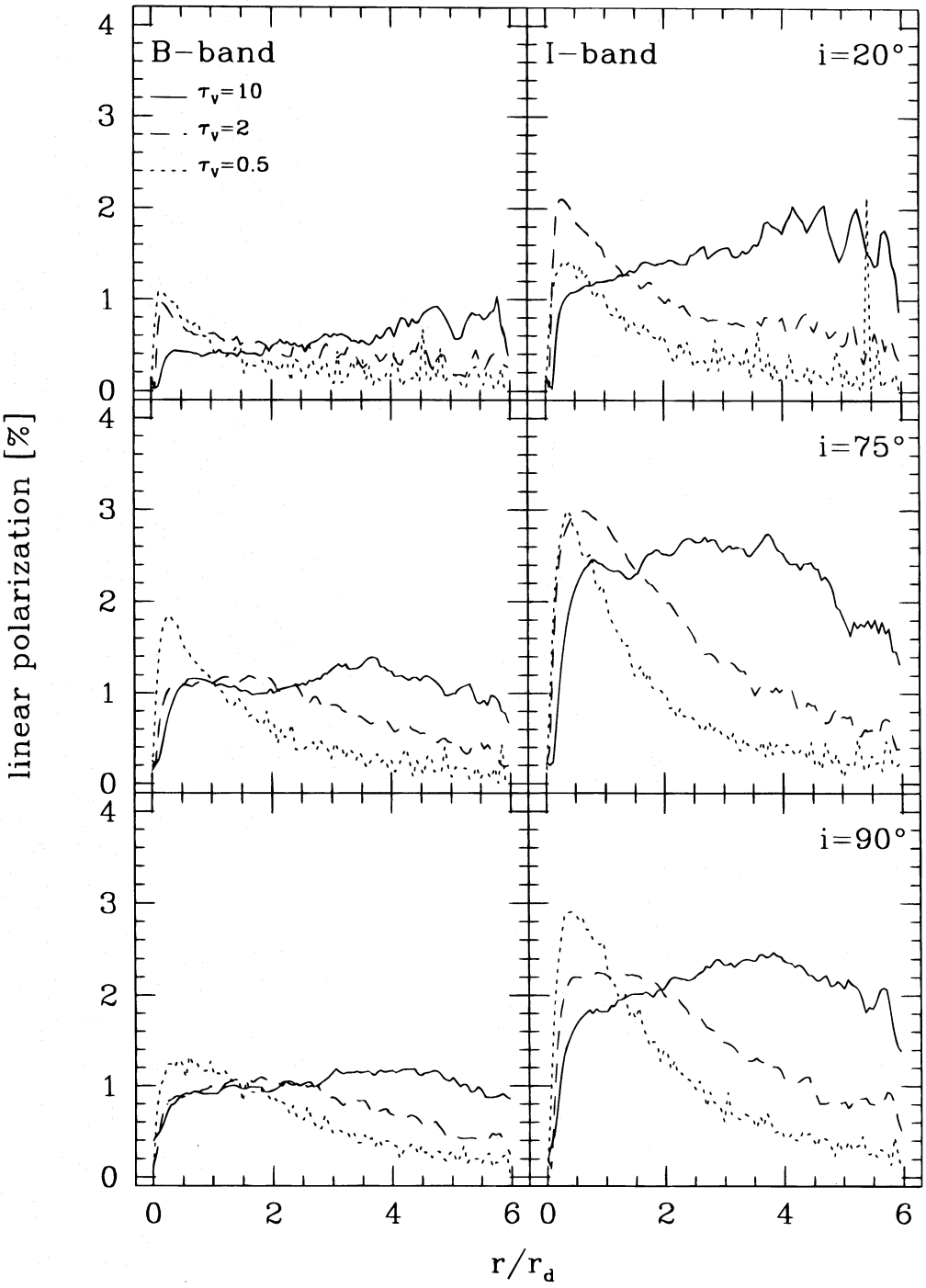

FIG. 9.—Linear polarization profiles along the major axis for BT05 models at inclinations 20°, 75°, 90°, for the *B* band (*left*) and *I* band (*right*). Profiles for $\tau_V(0) = 0.5, 2, 10$ are plotted.

Such effect is ascribed to the reduced extinction in the *I* band and the subsequent increase in the number of single scatterings. Most of the effects mentioned above are clearly depicted in Figure 9. The positions of the maxima coincide with regions where the local optical depth is ~ 1, similar to what was previously observed for color gradients.

If the number of scatterings is larger than 1, Mie scattering can in principle introduce a certain degree of local circular polarization. In all our models, the circular polarization degree is contained within the noise level and never appears at levels higher than 0.1%.

5. SUMMARY AND CONCLUSIONS

To study the extinction and polarization properties of dusty spiral galaxies, we have performed extensive Monte Carlo simulations using realistic galaxy models that include both a bulge and a disk component, simulating different Hubble types. The scattering properties are calculated from Mie's theory for each dust grain; in addition, we follow the radiative transfer of the four Stokes parameters. The grains are assumed to be spherical, with a power-law size distribution, and to consist of either graphite or silicates. This

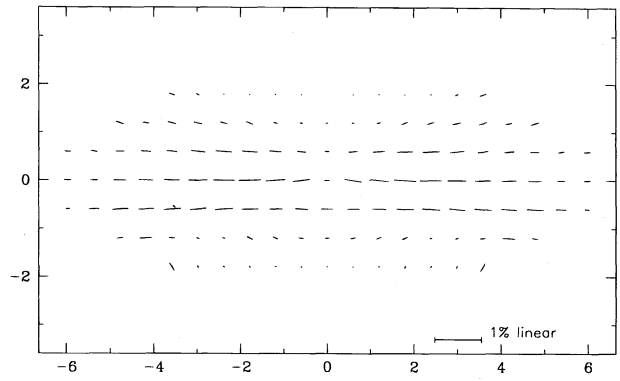

FIG. 10.—*B*-band BT05 model seen from 75°, with $\tau_B(0) = 5$ and a lower grain size cutoff $a_- = 0.15$ μm. Coordinates are measured in units of r_d.

enables us to produce both photometric and polarimetric maps of the galaxy for different optical depths, inclinations, and B/Ts; the main results derived from the analysis of such maps are summarized in the following.

In general, we find a very good agreement with the results of BFK, who used a series of approximations, described above, concerning luminosity profiles, total extinction, isophote shapes, and diameters.

We have shown that the overall effect of scattering (with respect to pure absorption) is to reduce the extinction for a given $\tau_V(0)$. Such decrement in the effective A_B is particularly evident in the central parts of bright bulges, as shown in Figure 4, although the extinction's fractional reduction is larger for late-type than for early-type spirals and increases with galactocentric distance. Sandwich models, often used in the literature, dramatically fail to reproduce the extinction–optical depth relation when scattering is properly considered, and they should not be used. From analysis of the $B-I$ color maps, we conclude that there is a net reddening of the galaxy due to dust even when scattering is included. In fact, the latter reduces, on average, the $B-I$ color by ~ 0.1 mag, a mild but appreciable effect. Radial color gradients are found to exist in regions where the optical depth is of order unity.

The degree of linear polarization produced by scattering is usually small (of the order of a few percent), but still practically measurable. The reasons for this behavior are that (1) there is a dilution effect by direct stellar (unpolarized) radiation; (2) the scattering region is usually illuminated from a large solid angle, thus photons with different histories enter the same beam; and (3) the distribution of grain sizes and materials degrades the coherence of the polarization. Most of the polarization comes from bulge light that is singly scattered by the outer layers of the disk. This is not surprising, of course, since the bulge is more compact and resembles a point source. The polarization degree increases with optical depth and with inclination, flattening out above $\sim 80°$. The polarization pattern is found to be perpendicular to the major axis, independent of the morphology, inclination, and optical depth; this result depends only on the optical properties of the dust grains and can be reversed only by shifting the lower limit for the dust size to much larger radii.

It is interesting to note that some galaxies do show linear polarization patterns similar to those of our models (Scarrott, Rolph, & Semple 1990; Fendt et al. 1996). Among them, late-type galaxies (NGC 5907, NGC 891) show polarization perpendicular to the major axis over the entire extent of the disk; early-type galaxies (NGC 4594, NGC 4565) instead show such polarization in the outer regions of the disk, whereas the central parts have polarization vectors consistent with dichroic absorption, that is, parallel to the major axis. When polarization vectors are perpendicular to the major axis, the observed degree of linear polarization is $\sim 1\%$, in agreement with our models.

Finally, there is little correlation between extinction and polarization degree, and there is a trend of increasing polarization from the *B* to the *I* band due to the reduced extinction in the *I* band and subsequent increase in single scatterings.

It is a pleasure to thank R.-J. Dettmar, E. Landi degl'Innocenti, M. Landi degl'Innocenti, M. Landolfi, and A. N. Witt for their interest and advice. We also acknowledge several stimulating discussions with F. Menard, A. Natta, L. K. Hunt, and the careful reading of an anonymous referee. S. B. wishes to thank the Arcetri chaos team for useful suggestions. Part of this study has been supported by the Programma Vigoni.

APPENDIX

DESCRIPTION OF THE MONTE CARLO CODE

With the Monte Carlo method, each event in a photon's life is determined by the probability distribution of a pseudorandom variable, $\rho(t)$, that describes the statistical weight of the variable t in the event and by extracting a random number

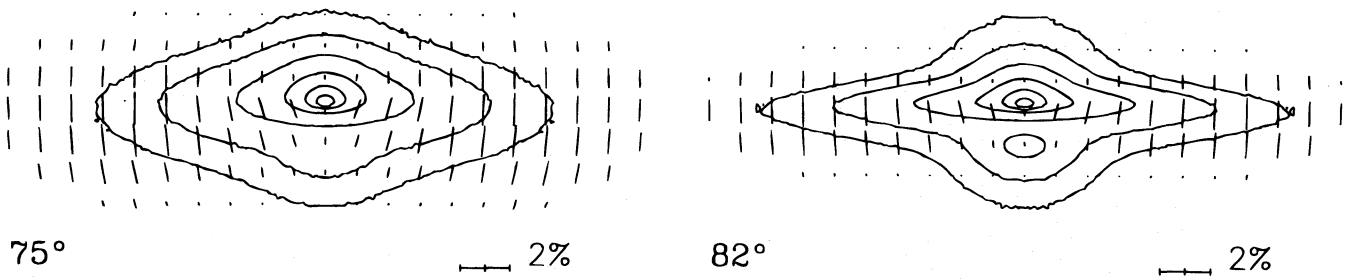

FIG. 11.—*B*-band polarization maps for a BT05 model, with $\tau_V(0) = 10$, for inclinations $i = 75°$ (*left*) and $i = 82°$ (*right*). Isophotes up to 25 *B*-mag arcsec^{-2} are superposed, spaced by 1 mag. The assumed face-on disk central brightness is 21.6 *B*-mag arcsec^{-2} (Freeman 1970).

$R \in [0, 1]$. The value t^* associated to the random number R according to $\rho(t)$ is given by the general Monte Carlo formula

$$\int_{t_{\min}}^{t^*} \rho(t)\,dt \Big/ \int_{t_{\min}}^{t_{\max}} \rho(t)\,dt = R\,, \tag{A1}$$

where $t_{\min}$ and $t_{\max}$ define the interval of possible values for t. In the following, R_i will indicate a random number between 0 and 1.

We adopt a Cartesian standard reference frame, with the z-axis along the galactic symmetry axis and the x- and y-axes in the equatorial plane. The y-axis coincides with the nodal line (intersection between sky plane and equatorial plane).

A1. EMISSION

In our models, photons are emitted by stars distributed in the galactic disk and bulge. The first step is to determine the coordinates of the star (i.e., the photon emission point) according to the stellar density distributions.

A1.1. *Bulge Emission*

Using the Jaffe law and substituting equation (2) into equation (A1), one finds a simple relation between the radial distance and a random number R_1:

$$\tilde{r}^* = r_b \frac{R_1}{[(n+1)/n] - R_1}\,, \tag{A2}$$

where n is the truncating factor of the Jaffe bulge and r_b is the scale radius. The $R^{1/4}$ and Jaffe distributions are relatively similar, but the relation between r_b and R_e depends on which physical parameters, and parts of the galaxy, we intend to match best. For our purpose, we need the relation fitting the luminosity within a given $\tilde{r}$, since this is the physical variable that we will directly associate with the Monte Carlo random numbers (this will be the case for the disk's radial distribution as well). In this sense, when uniformly sampled over the luminosity content, the best correspondence between the two distributions is found for $r_b = 1.16R_e$.

Then we determine the polar, θ, and azimuthal, ϕ, angles in spherical coordinates. With spherical symmetry we have

$$\phi^* = 2\pi R_2\,, \qquad \theta^* = \cos^{-1}(1 - 2R_3)\,, \tag{A3}$$

where R_2 and R_3 are two independent, random numbers. Thus the emission coordinates are

$$x_0 = \tilde{r}^* \sin\theta^* \cos\phi^*\,, \qquad y_0 = \tilde{r}^* \sin\theta^* \sin\phi^*\,, \qquad z_0 = \tilde{r}^* \cos\theta^*\,. \tag{A4}$$

In the more general case of axisymmetric ellipsoids, z_0 becomes

$$z_0 = \tilde{r}^* \epsilon \cos\theta^*\,, \tag{A5}$$

where ϵ is the ratio between the minor and major axes.

A1.2. *Disk Emission*

For an exponential disk (eq. [3]), the cylindrical radius of emission r^* can be found by numerically inverting

$$\frac{\int_0^{r^*} \exp(-r/r_d)\,r\,dr}{\int_0^{r_{\max}} \exp(-r/r_d)\,r\,dr} = \frac{1 - (1 + t^*)e^{-t^*}}{1 - (1 + m)e^{-m}} = R_1'\,, \tag{A6}$$

with $t^* = r^*/r_d$. From the azimuthal symmetry around the z-axis,

$$\phi^* = 2\pi R_2'\,. \tag{A7}$$

We calculate z using

$$\int_{-z_{\max}}^{z^*} Z\left(\frac{z}{z_d}\right)dz \Big/ \int_{-z_{\max}}^{z_{\max}} Z\left(\frac{z}{z_d}\right)dz = R_3'\,, \tag{A8}$$

where

$$Z(z/z_d) = \exp(-|z|/z_d) \qquad \text{or} \qquad \operatorname{sech}^2(z/z_d)\,. \tag{A9}$$

For the exponential law, we have

$$t^* = -\operatorname{sgn}(R_3' - \tfrac{1}{2}) \ln[\operatorname{sgn}(R_3' - \tfrac{1}{2})(1 - 2R_3')(1 - e^{-k}) + 1]\,; \tag{A10}$$

for the sech^2 law, the relation is

$$t^* = \tanh^{-1}[2(\tanh k)R_3' - \tanh k]\,, \tag{A11}$$

where $t^* = z^*/z_d$ and k is the vertical truncation factor. Thus,

$$x_0 = r^* \cos \phi^* , \qquad y_0 = r^* \sin \phi^* , \qquad z_0 = z^* . \tag{A12}$$

A1.3. *Direction*

If the radiation is emitted isotropically by stars, the longitude and colatitude of its direction are

$$\phi = 2\pi R_4 , \qquad \theta = \cos^{-1} (1 - 2R_5) , \tag{A13}$$

from which the direction cosines are computed:

$$l_0 = \sin \theta \cos \phi , \qquad m_0 = \sin \theta \sin \phi , \qquad n_0 = \cos \theta . \tag{A14}$$

We define the unit vector $\boldsymbol{v}_0 \equiv (l_0, m_0, n_0)$.

The stellar radiation is largely unpolarized, so we will assume for the initial Stokes parameters

$$\begin{pmatrix} I_0 \\ Q_0 \\ U_0 \\ V_0 \end{pmatrix} = \begin{pmatrix} 1 \\ 0 \\ 0 \\ 0 \end{pmatrix} . \tag{A15}$$

In the following, the Stokes parameters will be calculated assuming as reference direction the projection of the z-axis onto the plane normal to the photon's direction (for unpolarized radiation, eq. [A15] is true in all reference frames).

In summary, for the emission of each photon, we need to extract five random numbers, three for the coordinates of the point of emission and two for the direction of emission.

A2. DIFFUSION POINT

A photon emitted at (x_0, y_0, z_0) in direction $\boldsymbol{v}_0$ travels undisturbed until it collides with a dust grain. If undisturbed, the geometrical path within the dust distribution would be

$$\Gamma(t) = \begin{cases} x = x_0 + l_0 t \\ y = y_0 + m_0 t \\ z = z_0 + n_0 t \end{cases} \qquad (0 \le t < t_T) , \tag{A16}$$

where t_T is the t-value corresponding to the point of exit from the dust disk. The total optical depth τ_T along this path is

$$\tau_T = \frac{\tau_\lambda(0)}{2z_g} \int_0^{t_T} \frac{\rho^{(g)}(r, z)}{\rho_0^{(g)}} \, dt , \tag{A17}$$

where we have made use of equation (6) and $r = (x^2 + y^2)^{1/2}$. A fraction $e^{-\tau_T}$ of the photons will then emerge undisturbed from the system, while the remaining $1 - e^{-\tau_T}$ will be absorbed or diffused in other directions. The point of diffusion is associated with a random number R_6, which determines the total optical depth at the diffusion point according to

$$\int_0^{\tau} e^{-\xi} d\xi = R_6 \tag{A18}$$

or

$$\tau = -\ln (1 - R_6) . \tag{A19}$$

If $\tau > \tau_T$, the photon will exit without scattering. This procedure, however, is quite inefficient: if τ_T is small, most of the photons will exit directly. To overcome this problem, we have used the method of *forced scattering* introduced by Cashwell & Everett (1959; see also Witt 1977). With this method, the photon is split into two components: one, with intensity $I_1 = e^{-\tau_T}$, keeps traveling undisturbed and exits the dust disk; the other, with intensity $I_2 = 1 - e^{-\tau_T}$, is forced to scatter. Accordingly, equations (A18) and (A19) become

$$\int_0^{\tau} e^{-\xi} d\xi \Big/ \int_0^{\tau_T} e^{-\xi} d\xi = R_6 , \tag{A20}$$

$$\tau = -\ln [1 - R_6(1 - e^{-\tau_T})] , \tag{A21}$$

respectively. In the limit $\tau_T \to \infty$, τ tends toward the value for unforced scattering. The other Stokes parameters are scaled accordingly. Forcing the scattering also has the effect of reducing the noise in the resulting images, for the same total number of photons launches, but it is appreciably more time-consuming. We performed a series of trial simulations using a point

source embedded in spherical envelopes of optical opacity from 1 to 10. As a result of these tests, we adopted the following scheme in our code: the first scattering is always forced; the subsequent ones are forced only if $\tau_T > 1$. Among the various schemes tested, this one attains the best S/N within a given computational time.

We have used a threshold value $\tau_{\rm lim}$ for the optical depth: if a photon travels along a path with $\tau_T < \tau_{\rm lim}$, it is allowed to escape without being attenuated; the adopted value is $\tau_{\rm lim} = 10^{-4}$. Once τ, the optical depth of the impact event, has been calculated, the integral in equation (A17), but with t_1 instead of t_T, is inverted to find the value of t_1, the geometrical length traveled before impact. The coordinates of the first scattering are then

$$x_1 = x_0 + l_0 t_1 , \qquad y_1 = y_0 + m_0 t_1 , \qquad z_1 = z_0 + n_0 t_1 . \tag{A22}$$

A3. CHOICE OF DUST GRAIN

We now need to know the geometrical and optical characteristics of the dust particle located at (x_1, y_1, z_1). The probability for a photon to collide with a spherical grain of radius a, refractive index m, and material i is proportional to the product of the extinction cross section, $C_i^{\rm ext}$, and the grain number density, $n(a) \propto a^{-3.5}$ (MRN model). The differential collision probability can be written as

$$dP_i(a) \propto w_i a^{-3.5} C_i^{\rm ext} da , \tag{A23}$$

where w_i is the statistical weight of material i. Let us call $\chi_i(a)$ the function

$$\chi_i(a) = \int_{a_-}^{a} dP_i(a) , \qquad a \in [a_-, a_+] ; \tag{A24}$$

$\chi_i(a)$ can be normalized to unity dividing it by the value $\chi_{\rm tot}(a_+) = \sum_i \chi_i(a_+)$:

$$\bar{\chi}_i(a) = \chi_i(a)/\chi_{\rm tot}(a_+) . \tag{A25}$$

The function $\bar{\chi}_i(a)$ now has values between 0 and $\bar{\chi}_i(a_+)$. The interval [0, 1] can be divided into three subintervals for the three materials (Si, $C_\parallel$, $C_\perp$):

$$[0, \bar{\chi}_{\rm Si}(a_+)] , \qquad [\bar{\chi}_{\rm Si}(a_+), \bar{\chi}_{\rm Si}(a_+) + \bar{\chi}_{C_\parallel}(a_+)] , \qquad [\bar{\chi}_{\rm Si}(a_+) + \bar{\chi}_{C_\parallel}(a_+), 1] . \tag{A26}$$

In this way, by means of a random number R_7, we choose both the grain material and size. The grain size is found inverting the integral

$$\int_{a_-}^{a} \bar{\chi}_i(a)\, da + B_i = R_7 , \tag{A27}$$

where B_i is the value associated with the minimum value of each subinterval [$B_{\rm Si} = 0$, $B_{C_\parallel} = \bar{\chi}_{\rm Si}(a_+)$, etc.]. By knowing the wavelength and the material, we determine the complex refractive index, which, together with size, characterizes completely the optical properties of the grain.

A4. SCATTERING DIRECTION AND POLARIZATION TRANSFER

If $\boldsymbol{v}_0$ and $\boldsymbol{v}_1$ are unit vectors defining the propagation direction before and after scattering, respectively, we define $\boldsymbol{p}_{z0}$ as the unit vector indicating the projection of the positive z-axis (the galactic symmetry axis specified by the unit vector $\boldsymbol{k}$) onto the plane perpendicular to $\boldsymbol{v}_0$ at the scattering point. As mentioned before, $\boldsymbol{p}_{z0}$ defines the reference direction for the Stokes parameters of the incoming photon.

Two angles define $\boldsymbol{v}_1$ with respect to $\boldsymbol{v}_0$ (Fig. 12): the polar angle θ between $\boldsymbol{v}_0$ and $\boldsymbol{v}_1$, which is the actual angle of scattering, and the azimuthal angle ϕ between $\boldsymbol{p}_{z0}$ and $\boldsymbol{s}_0$, the projection of $\boldsymbol{v}_1$ onto the plane normal to $\boldsymbol{v}_0$. The vector $\boldsymbol{s}_0$ also lies in the scattering plane defined by $\boldsymbol{v}_0$ and $\boldsymbol{v}_1$. After some algebra, we derive

$$\boldsymbol{p}_{z0} = \frac{1}{\sqrt{1 - n_0^2}} (-l_0 n_0, -m_0 n_0, 1 - n_0^2) . \tag{A28}$$

Since the Mueller matrix elements are more easily defined for Stokes parameters referred to the scattering plane, we first have to perform a rotation about $\boldsymbol{v}_0$ and change to $\boldsymbol{s}_0$, the reference direction. The Stokes parameters of the incoming photon referred to the scattering plane are then

$$\begin{pmatrix} I_0' \\ Q_0' \\ U_0' \\ V_0' \end{pmatrix} = \begin{pmatrix} 1 & 0 & 0 & 0 \\ 0 & \cos 2\phi & \sin 2\phi & 0 \\ 0 & -\sin 2\phi & \cos 2\phi & 0 \\ 0 & 0 & 0 & 1 \end{pmatrix} \begin{pmatrix} I_0 \\ Q_0 \\ U_0 \\ V_0 \end{pmatrix} . \tag{A29}$$

With our assumptions, the phase function for polarized radiation is

$$\begin{aligned} \Phi(\theta, \phi) &= \frac{1}{\pi x^2 Q^{\rm sca}} \left(S_{11} + S_{12} \frac{Q_0'}{I_0'} \right) \\ &= \frac{1}{\pi x^2 Q^{\rm sca}} \left[S_{11}(\theta) + S_{12}(\theta) \left(\frac{Q_0}{I_0} \cos 2\phi + \frac{U_0}{I_0} \sin 2\phi \right) \right] \end{aligned} \tag{A30}$$

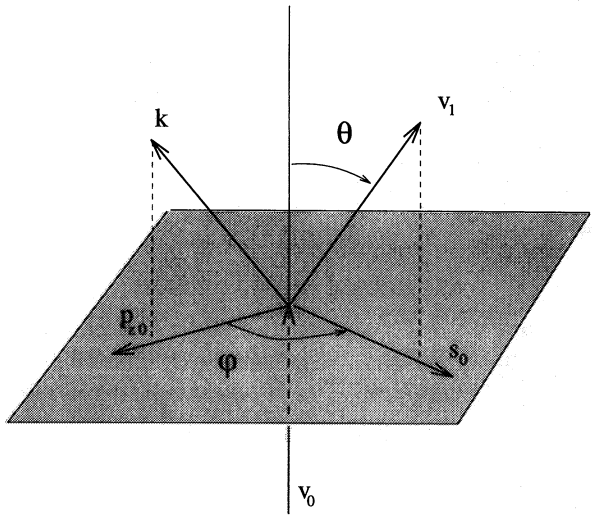

FIG. 12.—Scattering geometry. Vector $\boldsymbol{v}_0$ is the original direction of the photon, and $\boldsymbol{v}_1$ is the direction after scattering; the other vectors are defined in the text.

(van de Hulst 1957, p. 15), where

$$x = 2\pi a/\lambda\,, \qquad Q^{\rm sca} = C^{\rm sca}/\pi a^2\,. \tag{A31}$$

S_{11} and S_{12} are two elements of the Mueller matrix, which are functions only of θ (spherical grains), and $C^{\rm sca}$ is the scattering cross section (analogous to $C^{\rm ext}$). The angles θ and ϕ are distributed according to equation (A30). The phase function Φ is normalized so that

$$1 = \int_0^{2\pi} d\phi \int_0^{\pi} d\theta\, \sin\theta\, \Phi(\theta, \phi) = \int_0^{\pi} d\theta\, \sin\theta\, \tilde{\Phi}(\theta)\,, \tag{A32}$$

where

$$\tilde{\Phi}(\theta) = \int_0^{2\pi} \Phi(\theta, \phi)\, d\phi = \frac{2}{x^2 Q^{\rm sca}}\, S_{11}(\theta)\;; \tag{A33}$$

$\tilde{\Phi}$ depends only on θ, so θ can be derived from the Monte Carlo method, independently both of ϕ and of the polarization of the incident radiation. The scattering polar angle, θ, can be calculated from a random number R_8, inverting

$$\int_0^{\bar{\theta}} \tilde{\Phi}(\theta)\, \sin\theta\, d\theta = R_8\,. \tag{A34}$$

Substituting this value of θ into equation (A30), we can find $\bar{\phi}$ from

$$\int_0^{\bar{\phi}} \Phi(\bar{\theta}, \phi)\, d\phi \Big/ \int_0^{2\pi} \Phi(\bar{\theta}, \phi)\, d\phi = R_9\,, \tag{A35}$$

or

$$\frac{1}{2\pi}\left\{\bar{\phi} + \frac{S_{12}(\bar{\theta})}{2S_{11}(\bar{\theta})}\left[\frac{Q_0}{I_0}\sin 2\bar{\phi} + \frac{U_0}{I_0}(1 - \cos 2\bar{\phi})\right]\right\} = R_9\,. \tag{A36}$$

Using the values of $\bar{\theta}$ and $\bar{\phi}$ obtained before, we compute the direction cosines of $\boldsymbol{v}_1$:

$$\begin{aligned} l_1 &= \frac{\sin\bar{\theta}}{\sqrt{1 - n_0^2}}\,(-l_0 n_0 \cos\bar{\phi} + m_0 \sin\bar{\phi}) + l_0 \cos\bar{\theta}\,, \\ m_1 &= \frac{-\sin\bar{\theta}}{\sqrt{1 - n_0^2}}\,(m_0 n_0 \cos\bar{\phi} + l_0 \sin\bar{\phi}) + m_0 \cos\bar{\theta}\,, \\ n_1 &= \sqrt{1 - n_0^2}\,\sin\bar{\theta}\cos\bar{\phi} + n_0 \cos\bar{\theta}\,. \end{aligned} \tag{A37}$$

The new direction of propagation allow us to calculate the updated Stokes parameters after scattering (but still referred to the

scattering plane) by applying the Mueller matrix:

$$\begin{pmatrix} I_1'' \\ Q_1'' \\ U_1'' \\ V_1'' \end{pmatrix} = \begin{pmatrix} S_{11} & S_{12} & 0 & 0 \\ S_{12} & S_{11} & 0 & 0 \\ 0 & 0 & S_{33} & S_{34} \\ 0 & 0 & -S_{34} & S_{33} \end{pmatrix} \begin{pmatrix} I_0' \\ Q_0' \\ U_0' \\ V_0' \end{pmatrix} . \tag{A38}$$

It will be noted that equation (A38) is different from the usual relation for the scattered Stokes vector, since it does not include the spherical factor $1/k^2r^2$. The standard formulae (e.g., Bohren & Huffman 1983, eq. [3.16]) are derived for the distribution of the scattered electromagnetic fields, within the framework of the electromagnetic theory. In our description, the scattered photon is not distributed over the entire solid angle but, instead, deflected into a new single direction and attenuated by a factor equal to the albedo (which in Mie's approximation is independent of direction). If I_1' is the correct value of the scattered intensity, we have

$$I_1' = \tilde{\omega} I_0' = \tilde{\omega} I_0 , \tag{A39}$$

and the correct value of the Stokes vector after scattering will be

$$\begin{pmatrix} I_1' \\ Q_1' \\ U_1' \\ V_1 \end{pmatrix} = \frac{\tilde{\omega} I_0}{I_1''} \begin{pmatrix} I_1'' \\ Q_1'' \\ U_1'' \\ V_1'' \end{pmatrix} . \tag{A40}$$

The new Stokes parameters are defined with respect to $\boldsymbol{s}_1$, the unit vector that lies in the scattering plane and in the plane perpendicular to the new direction of propagation, $\boldsymbol{v}_1$ (Fig. 13); consistent with the convention adopted, we now have to calculate the Stokes parameters using as a reference $\boldsymbol{p}_{z1}$, the projection of the z-axis onto the plane normal to $\boldsymbol{v}_1$.

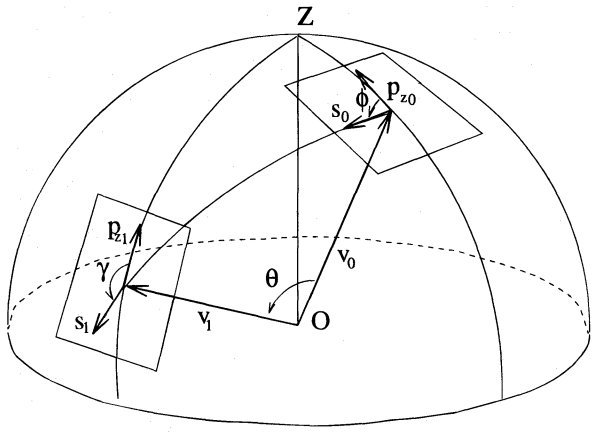

FIG. 13.—Scattering geometry in polar representation

The expression for $\boldsymbol{p}_{z1}$ is analogous to that for $\boldsymbol{p}_{z0}$ provided that we substitute $\boldsymbol{v}_1$ for $\boldsymbol{v}_0$. Since $\boldsymbol{s}_1$ lies in the scattering plane, it is parallel to the projection of $\boldsymbol{v}_0$ onto the plane normal to $\boldsymbol{v}_1$ (but with opposite direction), and we have

$$\boldsymbol{s}_1 \times [\boldsymbol{v}_0 - (\boldsymbol{v}_0 \cdot \boldsymbol{v}_1)\boldsymbol{v}_1] = 0 . \tag{A41}$$

From the previous relation, we have

$$\boldsymbol{s}_1 = \frac{1}{\sqrt{1 - (\boldsymbol{v}_0 \cdot \boldsymbol{v}_1)^2}} [l_1(\boldsymbol{v}_0 \cdot \boldsymbol{v}_1) - l_0, m_1(\boldsymbol{v}_0 \cdot \boldsymbol{v}_1) - m_0, n_1(\boldsymbol{v}_0 \cdot \boldsymbol{v}_1) - n_0] . \tag{A42}$$

The angle γ between $\boldsymbol{p}_{z1}$ and $\boldsymbol{s}_1$ is found using two other relations:

$$\cos \gamma = \boldsymbol{p}_{z1} \cdot \boldsymbol{s}_1 = \frac{n_1(\boldsymbol{v}_0 \cdot \boldsymbol{v}_1) - n_0}{\sqrt{1 - n_1^2}\sqrt{1 - (\boldsymbol{v}_0 \cdot \boldsymbol{v}_1)^2}} , \tag{A43}$$

$$\boldsymbol{v}_1 \sin \gamma = \boldsymbol{p}_{z1} \times \boldsymbol{s}_1 = \frac{m_0 l_1 - l_0 m_1}{\sqrt{1 - n_1^2}\sqrt{1 - (\boldsymbol{v}_0 \cdot \boldsymbol{v}_1)^2}} \boldsymbol{v}_1 . \tag{A44}$$

The Stokes parameters referred to $\boldsymbol{p}_{z1}$ will be calculated by applying a rotation by angle $-\gamma$:

$$\begin{pmatrix} I_1 \\ Q_1 \\ U_1 \\ V_1 \end{pmatrix} = \begin{pmatrix} 1 & 0 & 0 & 0 \\ 0 & \cos 2\gamma & -\sin 2\gamma & 0 \\ 0 & \sin 2\gamma & \cos 2\gamma & 0 \\ 0 & 0 & 0 & 1 \end{pmatrix} \begin{pmatrix} I'_1 \\ Q'_1 \\ U'_1 \\ V'_1 \end{pmatrix} . \tag{A45}$$

In summary, every diffusion event requires four random numbers, one to locate the diffusion point, one for the optical characteristics of the grain, and two to determine the new direction of propagation.

A5. IMAGING

After N scatterings, the photon parameters satisfy the exit conditions. The final parameters are the point of last scattering (x_N, y_N, z_N), the exit direction $\boldsymbol{v}_N = (l_N, m_N, n_N)$, and the exit Stokes parameters (I_N, Q_N, U_N, V_N).

Our galactic models have two symmetries that can be used to reduce the computational time: (1) axial symmetry around the z-axis and (2) planar symmetry about the equatorial (x-y) plane. If we look at the galaxy from a point at infinite distance in the x-z plane, given the axial symmetry, we perform a rotation around the z-axis and align $\boldsymbol{v}_N$ parallel to the x-z plane. After rotation, the exit direction can be identified by the new coordinates of the point of last scattering, (x, y, z), and by the polar angle θ only (we omit the subscript N for simplicity). The corresponding Stokes parameters (I, Q, U, V) will be the same as (I_N, Q_N, U_N, V_N) because a rotation around the z-axis does not modify the relative orientation of the wave electric field and the z-axis. Because of the axial symmetry, for each photon exiting from (x, y, z) with direction θ and parameters (I, Q, U, V) we can add another photon exiting from $(x, -y, z)$ with the same direction and parameters $(I, Q, -U, -V)$. We can then exploit the planar symmetry: for each photon exiting from (x, y, z) with direction θ and parameters (I, Q, U, V), we add a photon with $(x, y, -z)$, direction $\pi - \theta$, and parameters $(I, Q, -U, V)$. Using these symmetries we gain, therefore, a factor of 4 in the number of photons.

To produce maps of the galaxy as seen from different inclinations, we select the photons, after their exit, according to their θ-direction. This is done by dividing the whole solid angle into N_B latitudinal bands of equal solid angle. All the photons with exit directions within a given band will contribute to the image relative to that range of θ-values. Note that this introduces a finite resolution in inclination: for example, with our standard ($N_B = 15$) sampling, the most face-on image includes inclinations ranging from 0° to 30°, while the edge-on case includes inclinations between 86° and 94°. Having already exploited the planar symmetry, images with inclinations θ and $\pi - \theta$ will be identical. Finally, the photons pertaining to a certain inclination band are projected onto the plane of the sky, according to their point of last scattering and direction.

The final result consists of N_B images for each Stokes parameter. Linear polarization maps are obtained by calculating, for each pixel, the linear polarization and the polarization angle,

$$P = \sqrt{Q^2 + U^2}/I , \qquad \psi = \tfrac{1}{2} \arctan (U/Q) + \psi_0 , \tag{A46}$$

respectively, where ψ_0 is defined in Calamai, Landi degl'Innocenti, & Landi degl'Innocenti (1975).

REFERENCES

Bianchi, S. 1995, Laurea thesis, Univ. Firenze
Block, D. L., Witt, A. N., Grosbøl, P., Stockton, A., & Moneti, A. 1994, A&A, 288, 383
Bohren, C. F., & Huffman, D. R. 1983, Absorption and Scattering of Light by Small Particles (New York: Wiley)
Burstein, D., Haynes, M. P., & Faber, S. M. 1991, Nature, 353, 515
Byun, Y. I., Freeman, K. C., & Kylafis, N. D. 1994, ApJ, 432, 114 (BFK)
Calamai, G., Landi degl'Innocenti, E., & Landi degl'Innocenti, M. 1975, A&A, 45, 297
Cashwell, E. D., & Everett, C. J. 1959, A Practical Manual on the Monte Carlo Method for Random Walk Problems (New York: Pergamon)
Chołoniewski, J. 1991, MNRAS, 239, 939
de Vaucouleurs, G. H. 1959, in Handbuch der Physik, Vol. 53, ed. S. Flugge (Berlin: Springer), 275
de Vaucouleurs, G. H., de Vaucouleurs, A., Corwin, H. G., Buta, R. J., Pature, G., & Forqué, P. 1991, Third Reference Catalogue of Bright Galaxies (New York: Springer)
Disney, M. J., Davies, J. I., & Phillipps, S. 1989, MNRAS, 239, 939
Draine, B. T., & Lee, H. M. 1984, ApJ, 285, 89
Elvius, A. 1956, Diffraction of Light by Interstellar Particles in Spiral Galaxies (Stockholm Obs. Ann., 18, No. 9) (Stockholm: Almqvist & Wiksell)
Evans, R. 1994, MNRAS, 266, 511
Fendt, C., Beck, R., Lesch, H., & Neininger, N. 1996, A&A, in press
Fischer, O., Henning, Th., & Yorke, H. W. 1994, A&A, 284, 187
Freeman, K. C. 1970, ApJ, 160, 811
Giovanelli, R., Haynes, M. P., Salzer, J. J., Wegner, G., da Costa, L. N. D., & Freudling, W. 1994, AJ, 107, 2036
Gledhill, T. M., & Scarrott, S. M. 1989, MNRAS, 236, 139
Henyey, L. G., & Greenstein, J. L. 1941, ApJ, 93, 70
Holmberg, E. 1958, A Photographic Photometry of Extragalactic Nebulae (Medd. Lunds Astron. Obs., Ser. 2, No. 136) (Lund, Sweden: C. W. K. Gleerup)
Jaffe, W. 1983, MNRAS, 202, 995
Kylafis, N. D., & Bahcall, J. M. 1987, ApJ, 317, 637
Martin, P. G., & Rouleau, F. 1991, in Extreme Ultraviolet Astronomy, ed. R. F. Malina & S. Bowyer (Elmsford, NY: Pergamon)
Mathis, J. S., Rumpl, W., & Nordsiek, K. H. 1977, ApJ, 217, 425 (MRN)
Menard, F. 1989, Ph.D. thesis, Univ. Montréal
Ohta, K., & Kodaira, K. 1995, PASJ, 47, 17
Peletier, R. F., Valentijn, E. A., Moorwood, A. F. M., & Freudling, W. 1994, A&AS, 108, 621
Rieke, G. J., & Lebofsky, M. J. 1985, ApJ, 288, 618
Sandage, A., & Tammann, G. A. 1981, A Revised Shapley-Ames Catalog of Bright Galaxies (Carnegie Inst. Washington Publ. 635)
Scarrott, S. M., Rolph, C. D., & Semple, D. P. 1990, in IAU Symp. 140, Galactic and Intergalactic Magnetic Fields, ed. R. Beck, P. Kronberg, & R. Wielebinski (Dordrecht: Kluwer), 254
Shurcliff, W. A. 1962, Polarized Light (Cambridge, MA: Harvard Univ. Press)
Spitzer, L. 1978, Physical Processes in the Interstellar Medium (New York: Wiley)
Valentijn, E. A. 1990, Nature, 346, 153
———. 1994, MNRAS, 266, 614
van de Hulst, H. C. 1957, Light Scattering by Small Particles (New York: Dover)
van der Kruit, P. C., & Searle, L. 1981, A&A, 95, 105
Wainscoat, R. J., Freeman, K., & Hyland, A. R. 1989, ApJ, 337, 163
Wielebinski, R., & Krause, F. 1993, A&A Rev., 4, 449
Witt, A. N. 1977, ApJS, 35, 1
Young, P. J. 1976, AJ, 81, 807